Applied Clay Science 195 (2020) 105722

Contents lists available at ScienceDirect

Applied Clay Science

journal homepage: www.elsevier.com/locate/clay

Research Paper

Kaolins of high iron-content as photocatalysts: Challenges of acidic surface modifications and mechanistic insights

Katalin Győrfi[a], Veronika Vágvölgyi[b], Balázs Zsirka[a,*], Erzsébet Horváth[a,*], Róbert K. Szilágyi[c], Kornélia Baán[d], Szabolcs Balogh[e], János Kristóf[b]

[a] Institute of Environmental Engineering, University of Pannonia, P.O. Box 158, Veszprem 8201, Hungary
[b] Department of Analytical Chemistry, Institute of Chemistry, University of Pannonia, P.O. Box 158, Veszprem 8201, Hungary
[c] Department of Chemistry and Biochemistry, Montana State University, P.O. Box 173400, Bozeman, MT 59717, United States
[d] Department of Applied and Environmental Chemistry, Institute of Chemistry, University of Szeged, PO Box 652, 6701 Szeged, Hungary
[e] NMR Laboratory, Institute of Chemistry, University of Pannonia, P.O. Box 158, Veszprem 8201, Hungary

ARTICLE INFO

Keywords:
High iron-content kaolin
Acid treatment
Al defect sites
Acid/base properties
Photochemical activity
Solid state ^{27}Al NMR

ABSTRACT

Surface modifications of natural kaolins (Felsőpetény, Hungary) with iron-content up to 9% (*m/m*) were carried out by varying acid concentration (5, 8 and 11 M HCl) and treatment time (1, 3 and 6 h) in order to evaluate the influence of treatment conditions on photochemical activity, amount of low coordinate Al defect sites, porosity, and acid/base character of the surface. Nitrogen adsorption and temperature-programmed desorption measurements showed that the acid treatment slightly reduced the pore volume and the surface area, while the average pore diameter and the number of acidic centers were increased. Solid-state ^{27}Al NMR spectroscopy demonstrated the presence of mechanistically relevant Al defect sites. The distribution, concentration, and particle size of the iron oxide co-minerals were found to be influential to photochemical activity. Greater than 90% photochemical degradation efficiency of oxalic acid can be achieved by acid-treated samples upon 3 h exposure to 8 M HCl solution with good reproducibility.

1. Introduction

Kaolinite is a 1:1 type layered, dioctahedral aluminosilicate with a formula of $Al_2Si_2O_5(OH)_4$ that manifests a two-dimensional arrangement of Si-tetrahedra (T-sheet) and Al-octahedra (O-sheet). Inner OH-groups (iOH) are located in the plane common to the T- and O-sheets. The inner surface OH-groups (isOH) form strong H-bonds with the oxide anions from the adjacent T-sheet in the crystalline phase. The OH-groups located on the outermost surface of the kaolinite particles and along broken edges are the outer surface OH-groups (osOH). The aforementioned H-bonds are arranged approximate parallel with the crystallographic 'c' axis in a book-type crystalline morphology. The basal distance is *ca.* 7.1 Å. Thus, the kaolinite can be considered as a 2D-material that under defect site free conditions is capped with hexacoordinate $Al(osOH)_3$ (^{VI}Al) and tetracoordinate $Si(O)_3$ (^{IV}Si) surface layers (Bergaya et al., 2006).

Functionalization of surface-exposed groups, intercalation, exfoliation, mechanochemical activation, acidification, and thermal treatment are among the commonly employed methods to induce or alter reactivity. Here, we combined various surface modification procedures for enhancing natural kaolin-based materials with a goal to develop adsorbents and photocatalysts (Bergaya et al., 2006). A relevant discovery of the last decade is the identification of the photochemical activity of the kaolinite family of minerals. While the exact physico-chemical background of their activity is not well understood to date, the impact of developing novel environmental remediation technologies is unquestionable (Stebbins et al., 2000; Ulicna et al., 2013; Gleizes et al., 2014; dos Santos et al., 2017; Szabó et al., 2017).

Natural kaolins always contain mineral contaminants to kaolinite. Goethite, hematite, and anatase contaminants are of particular interest for photocatalysis. For example, goethite-containing kaolins can be utilized for the photochemical decomposition of persistent pesticides (Menager and Sarakha, 2012). The photochemical activity of red clay (*a.k.a.* taua that typically contains kaolinite, halloysite, iron oxide and iron oxyhydroxide) was reported for decomposing methylene blue by irradiation with UV light of $\lambda_{max} = 418$ nm (dos Santos et al., 2017). Others studied the photocatalytic hydrogen production and the photodegradation of dye pollutants (Gupta et al., 2007; Lopes et al., 2019) using surface-modified natural red clay mineral (Liu et al., 2018). While the fundamental physico-chemical background of the photochemical

* Corresponding authors.
E-mail addresses: zsirkab@almos.uni-pannon.hu (B. Zsirka), erzsebet.horvath@gmail.com (E. Horváth).

https://doi.org/10.1016/j.clay.2020.105722
Received 7 April 2020; Received in revised form 5 June 2020
Available online 20 June 2020

activity of kaolinite is still under intense research, kaolin samples showed photochemical activity in decomposition of methylene-blue and toluene, independently of the nature of contaminants (Kibanova et al., 2011). These results are also supported by our earlier observations (Szabó et al., 2017). We also found that the morphology and the presence of defect sites strongly influence porosity and the acid/base properties (Zsirka et al., 2017a).

The catalytic activity of natural kaolin (Üzüm et al., 2009) or synthetic kaolinite (Zhu et al., 2019) minerals can be correlated with the Brønsted-Lewis acidity of the surface and the presence of redox-active substitutions, such as transition metal ions. The variability in composition, morphology, and spectroscopic features can be an advantage over the zeolite-based catalysts in terms of selectivity, activation energy, and the synthesis of composites and hybrids (Menager and Sarakha, 2012). The acid/base character of the kaolinite surface can be tuned by the external chemical environment. The surface acidity of untreated natural kaolin has been reported to have a pH value as low as 4.5 due to dangling bonds and incomplete coordination environment at the edge sites (Conley and Althoff, 1971). As an analogue of the O-sheet, ^{1}H NMR studies identified six different acid/base chemical environments for γ-alumina (Barrow et al., 2016) that we utilized for describing the acid/base features of the surface on the basis of modified Knötzinger-Ratnasamy-type nomenclature (Tsyganenko and Mardilovich, 1996). A surface with acidic character shows the accumulation of a positive charge in the vicinity of O-defect sites, while for a basic surface the overall charge is negative or neutral due to Al and less commonly Si defect sites (Barrow et al., 2016). To date, only limited or contradictory ^{1}H NMR information is available for kaolinite family minerals due to their varied chemical environments with high osOH concentration and diverse morphology. TPD measurements were reported for various Jordanian silicates, zeolites, bentonites, and red- and white-kaolins (Alsawalha, 2016; Kumar et al., 2013; Novikova et al., 2014; Solyman and Betiha, 2014); however, parallels are limited with our data due to the different sample pre-treatment and measurement conditions.

Defect sites expected to play a key role in catalytic processes. Here, the concentration and acid/base properties of the defect sites are of high importance. A detailed structural study of clay minerals and less-ordered Al-oxides revealed the presence of Al sites that differ from the ideal octahedral coordination (^{VI}Al). Five- (^{V}Al) and four-coordinate (^{IV}Al) Al sites can be identified in fluoride-containing aluminosilicate glasses from ^{27}Al 3QMAS NMR spectra (Stebbins et al., 2000). Synthesis of amorphous Al-oxide layer on Al-thin films revealed that the temperature of spontaneous film formation influences the ^{IV}Al:^{V}Al:^{VI}Al ratio (Gleizes et al., 2014). They concluded that sample preparation at low temperatures prefers the formation of low coordinate Al sites, while at higher temperatures the ideal octahedral coordination prevails. Furthermore, pH and temperature may also influence the Al-coordination as shown for Czech kaolins (Ulicna et al., 2013) by showing that even the untreated, natural kaolin samples contained low amounts of ^{V}Al. Contrary to the above-mentioned thin-film study, heat treatment favored the formation of ^{IV}Al, but alkaline hydrolysis resulted in the disappearance of ^{V}Al giving high ^{IV}Al/^{VI}Al ratio of 9/1.

Iron ions in kaolin samples can be present in the forms of co-mineral oxides, oxyhydroxides, carbonates, structural ions by Al or less often Si/Fe substitutions, or part of the adsorbed organic matter. Electron microscopy images showed that the structural iron is randomly distributed in the kaolinite crystal (Jepson and Rowse, 1975) in parallel with ^{27}Al MAS NMR studies (Schroeder and Pruett, 1996). A straightforward way of removing the Fe contaminants is by acid treatment. However, acids can attack the aluminosilicate structure (Bryant and Buller, 1990), leading occasionally to the formation of amorphous aluminosilicate precipitates. According to literature, the use of HCl has a negligible effect on the silicate structure (Schroeder and Pruett, 1996); thus, acid treatment can be used to tune the amount and phase of co-minerals. This is in contrast to using HNO_3 or H_2SO_4, which can degrade the aluminosilicate structure (Panda et al., 2010; Ajemba et al., 2013). We emphasize the potential of controlled HCl exposure of kaolin samples for creating surface defect sites.

The consideration of kaolins with co-mineral contaminants of photocatalytic nature, especially hematite (band gap 2.1 eV), goethite and/or titanium dioxide (band gap 3.2 eV) is beneficial for defining parameters influencing the photochemical activity for environmental and technological applications. The cooperativity in the photochemical activity of TiO_2, Fe_2O_3, and halloysite, as nanocomposites has been demonstrated (Szczepanik et al., 2017). It is also desirable to understand the role of kaolinites in soils and sediments with respect to self-cleaning, such as the natural degradation of pollutants in soils/surface waters. These can lead to the development of new cost-efficient environmental technologies based on clays. Our work demonstrates the photochemical activity of kaolinite nanocomposites by tuning the iron-containing co-mineral contaminants. At the same time, we call attention to the challenges of chemical analysis associated with the structural and surface characterization of these (nano)materials.

2. Experimental and methods used

2.1. Sample preparation

The sample compositions, designations, preparation and surface treatments are given below. Variations in humidity, loss on ignition, and Fe-content were as expected for natural samples.

2.1.1. Crystalline sample, K

Natural kaolin from Felsőpetény, Hungary; composition in (*m/m*)% 56 SiO_2, 22 Al_2O_3, 5.6 Fe_2O_3, 1.0 TiO_2, 0.3 CaO, 0.6 MgO, 1.1 K_2O, 0.1 Na_2O; humidity: 10–12 (*m/m*)%; loss on ignition: 8–9 (*m/m*)%; acid (11 M HCl) soluble iron content 5.1 (*m/m*)%, in Fe_2O_3; structural iron content: 0.56 (*m/m*)%, in Fe_2O_3.

2.1.2. Exfoliated nanokaolinite, Knano

Prepared by exchange intercalation and exfoliation (Zsirka et al., 2015); precursor (K + KAc) synthesis using kaolin:potassium acetate (*m/m*)% ratio of 70:30 for 5 days of agitation followed by drying at 110 °C (92–94% intercalation efficiency); first exchange intercalation (K + EG) using 1 g of K + KAc and 5 mL dry ethylene-glycol (EG) by stirring for 3 h at 150 °C followed by centrifugation, and drying (92–94% intercalation efficiency); second exchange intercalation (repeated three times) using dry *n*-hexylamine (K-HA), 1 g of K-EG + 5 mL hexylamine, stirring at room temperature for 60 h in Ar atmosphere followed by centrifugation and drying (96% intercalation efficiency); last exfoliation step is by washing with toluene of 1 g K-HA + 5 mL toluene, stirring at room temperature for 5 h, centrifugation, and drying at room temperature (38% exfoliation efficiency); final surface cleaning by washing with isopropanol, acetone, and MilliQ-water.

We adopted a nomenclature (K-X−Y) to designate 5, 8, and 11 M HCl concentrations of 10 mL HCl(aq) (X) and 1, 3, and 6 h treatment period (Y) of ~2.5 g kaolin sample with particle size < 125 µm. Correspondingly, Knano-11-6 corresponds to ~2.5 g of nanokaolinite from exchange intercalation and exfoliation treated with 10 mL of 11 M HCl(aq) solution for 6 h. The acid-treated samples were washed by 2 × 15 mL of MilliQ water to remove surface-adsorbed acid, then dried and grounded.'-W′ indicates additional washing after acid treatment using 5 × 15 mL of MilliQ water, drying, grinding, resting for 24 h. The K-8-3-W sample with an additional two weeks of air-drying was utilized in seven parallels of photochemical testing. We wish to emphasize the importance of secondary sample treatments to acid treatment due to their influence on photochemical activity (Ding et al., 1999).

2.2. Photochemical activity

Surface-treated kaolinite (35 mg) was added to 35 mL of 1 mM

$(COOH)_2$ aqueous solution. After mixing in the dark for 20 min, the non-adsorbed oxalic acid (c_{aq}) was determined by permanganometric titration (1 mM $KMnO_4$). The same sample suspension was irradiated using a λ_{max} = 365 nm UV light for 4 h while stirring. The efficiency of decomposition was calculated by considering the amount of initial, adsorbed, and residual (c_{photo}) oxalic acid.

2.3. Structure elucidation methods

2.3.1. X-ray powder diffraction

X-ray powder diffraction (XRD) measurements were carried out using a Philips PW 3710-type instrument (CuKα radiation, λ = 1.54056 Å, 50 kV, 40 mA), in the 5–70° 2θ range with a scanning speed of 0.02 degree/s and 1 s integration time. The finely ground samples were loaded into 'back-packed mounts' in order to minimize preferential particle orientation.

2.3.2. NMR spectroscopy

Spectra were recorded using a Bruker Avenece 9.4 T spectrometer equipped with a 4 mm MAS BBO probe-head. The spinning frequency was varied between 8 and 12 kHz to differentiate peaks and spinning sidebands. Chemical shifts were referenced to an external standard of pure $Al(NO_3)_3$(s). Samples were packed under Ar in a Si_3N_4 rotor and closed with a Kel-F cap. The signal shape and intensity are influenced by quadrupole effects as a result of coupling between the nucleus (I_N (^{27}Al) = 5/2) and the electric field gradient as a function of the chemical environment. With a sufficiently short pulse $\tau = \pi/(2(I + 1/2))$ ($\pi/12$ for ^{27}Al) close to quantitative response can be achieved from the different environments (Fenzke et al., 1984). The $\pi/2$ pulse time was determined in the liquid phase using the reference sample. The $\pi/12$ pulse was 1.33 µs. In a typical ^{27}Al MAS experiment, 128 scans were acquired. The relaxation delay was 5 s. Dipolar broadening by ^{1}H direct and/or scalar coupling was not noticeable, ^{1}H decoupling was not used. Due to the small amount of H^+ in the vicinity of aluminum ions, the ^{27}Al CP MAS experiments showed low sensitivity and usually 512 scans were collected. Hartmann-Hahn matching conditions were determined for the CP MAS measurements. The ^{27}Al MAS spectra showed a small background signal at 109 ppm. Probehead background signal in the ^{1}H MAS measurements was effectively removed using the rotor-synchronized Hahn-echo T_2 filter sequence with a 36 s/12,000 = 2.99 ms delay. (Hou et al., 2002)

2.3.3. SSA/porosity and TPD measurements

The specific surface area (SSA) and pore volume/size distribution in the micropore (1.7–2 nm), mesopore (2–50 nm), and the macropore (50–100 nm) diameter ranges were determined by N_2 (Messer 99.995%) adsorption/desorption isotherms using the Brunauer-Emmett-Teller (BET) method and Barret–Joyner–Halenda (BJH) model, respectively. These were measured using a Micromeritics ASAP 2000-type instrument on samples of ~1 g, outgassed in vacuum at 60 °C. Pre-treatment was completed when the vacuum pressure dropped below 10^{-5} torr.

The characterization of the acid/base surface sites was carried out using temperature-programmed desorption experiments (TPD) with CO, CO_2, and NH_3 probe gases in a BELCAT-A type instrument. In order to remove organic surface contaminants and adsorbed water, the samples were heated in a He flow at 350 °C prior to the measurements. The pre-treatment temperatures were determined by thermoanalytical experiments (Vágvölgyi et al., 2020). Afterwards, the samples were cooled back to 50 °C (CO_2) and 100 °C (NH_3). Samples for the CO adsorption measurements were initially treated in a stream of H_2 using a 10 °C/min heating rate up 350 °C, holding for 30 min in order to reduce the surface exposed Fe^{3+} ions to metallic state that enhances CO binding and then cooled in He gas to 50 °C. After 30 min of gas adsorption, the excess gases were removed by a He flow and the temperature was increased to 350 °C at a rate of 10 °C/min. The desorbed gases were detected by means of a thermal conductivity detector (TCD).

2.3.4. TEM/STEM studies

Transmission electron microscopic (TEM) investigations were carried out using an FEI Talos F200X electron microscope with an X-FEG electron source, operated at 200 kV accelerator potential. SuperX EDX detector was used for the energy dispersive X-ray mode. TEM images were recorded in normal and scanning modes. The samples were prepared for an aqueous dispersion (MilliQ water) onto a lacy carbon-coated copper grid and dried at 60 °C.

3. Results and discussion

3.1. X-ray powder diffraction measurements of acid treated sample

Fig. 1A shows the 5–70° 2θ angle region of XRD data that defines the composition of the main phases and mineral contaminants. Significant amounts of illite, quartz, and small amounts of orthoclase and albite (not marked) co-minerals were found. Fig. 1B shows a narrower 2θ angle region that is informative for goethite and hematite with low-intensity peaks, while high-intensity bands are presented separately in Fig. 1C. We detected only negligible perturbations in peak positions and intensities upon acid treatment, which indicates a lack of change in the overall structure of the aluminosilicate frame. Fig. 1C clearly shows that the acid treatment only affects the intensity of the Fe-containing co-minerals (goethite and hematite) bands. By employing 11 M HCl solution for a few hours, practically all Fe co-minerals were removed without affecting the kaolinite structure. However, a small amount of goethite remains detectable by XRD after treatments with 5 M (K-5) or 8 M (K-8) HCl, independently of the treatment time. ICP analysis showed an iron concentration variation of 1.5–1.8% (*m/m*) between the acid-treated K-5-6 and K-11-6 samples. The amount of hematite was significantly reduced upon treatment with 5 M HCl(aq) for 1 h (K-5-1), and it was practically eliminated during a prolonged treatment (see Fig. 1C).

In addition to the iron co-minerals (goethite and hematite) in sample K, the presence of structural iron must also be considered, which was estimated to be 0.56% (*m/m*) as Fe_2O_3 or 0.39% (*m/m*) as Fe atom. Notably, the additional acid treatment using 20% H_2SO_4(aq) of K-11-6 did not lower the structural iron content, which indicated that the dominant part of the structural iron was not surface exposed.

Defect sites at the broken edges of TO-type clay minerals (Jia et al., 2019) allow for cation binding through ion exchange. ICP analysis showed the presence of 0.103 ± 0.003% (*m/m*) Al^{3+} in solution (~2 mM) independently of acid concentration and treatment time. This suggests that due to the high Fe^{3+} concentration in the acidic solution, a certain part of the edge-type Al may be exchanged for Fe^{3+} ions. Plausibly, iron ion at the edge sites may form a goethite-like, iron oxyhydroxide phase (Jia et al., 2019).

3.2. Morphology variation and elemental distribution maps

Sample morphology and distribution of iron-containing contaminants were studied by TEM. In the case of the untreated sample K, the TEM image in Fig. 2 shows the presence of TiO_2 (anatase) and well-crystallized iron co-minerals (Fig. 2A1 and 2A2). Treatment with 5 M HCl(aq) for 3 h leaves island-like and fibrous goethite residues (~500 nm) on the surface (Fig. 2B1 and 2B2). The sample treated with 8 M HCl(aq) for the same period followed by washing with water displays agglomerated particles of under 500 nm (Fig. 2C1 and 2C2). On the contrary, treatment with *cc.* HCl(Aq) for 6 h completely removed all iron-particles. The finely distributed amorphous iron contamination came from adsorption after drying (Fig. 2D1 and 2D2). TiO_2 concentration did not change and remained present in less than 1% (*m/m*) after the acid treatment in all samples. Its particle size and distribution were comparable to those of the iron co-minerals. Our acid-treated,

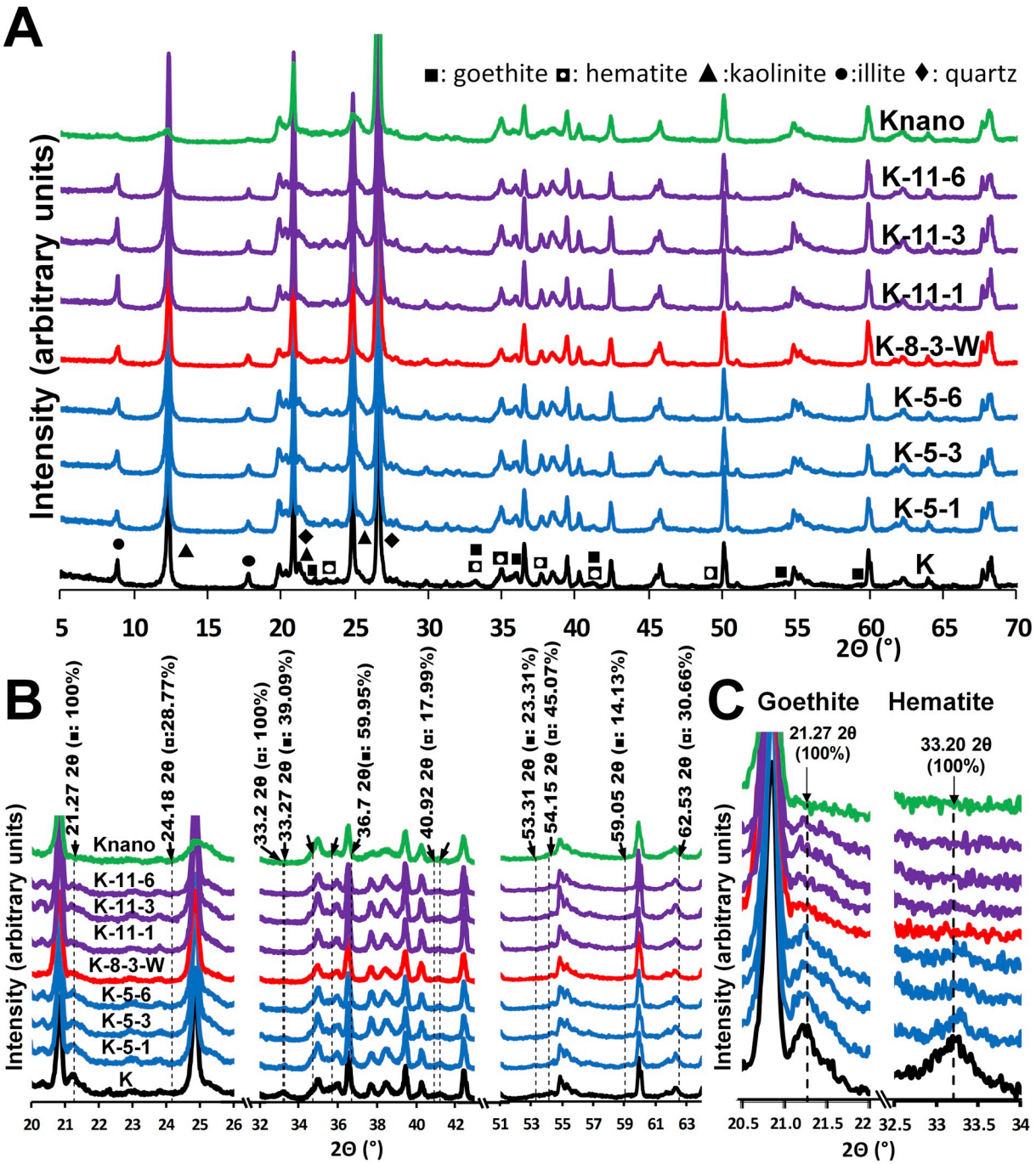

Fig. 1. Comparison of powder X-ray diffraction data demonstrating the effects of acid treatment of kaolin on co-mineral composition of K, K-5-1, K-5-3, K-5-6, K-8-3, K-11-1, K-11-3, K-11-6 and Knano. (PDF numbers: Hematite (00–033-0664), Goethite (01–081-0464), Kaolinite (00–014-0164), and Illite (00–026-0911)).

natural kaolin can be considered as a three-component nanocomposites system: kaolinite-Fe_2O_3-TiO_2. We emphasize that we utilize natural, earth-abundant raw materials that have economic and sustainability benefits over artificially synthesized materials (Fida et al., 2015). As we show below, the photochemical activity of natural kaolins can be tuned by adjusting the concentration and morphology of iron oxide/oxy-hydroxide co-minerals and nanoparticles.

3.3. Local structure information from solid-state ^{27}Al NMR measurements

The change in the coordination environment of the Al sites as the result of acid treatment was investigated by ^{27}Al Magic-Angle Spinning (MAS) and cross-polarization (CP) NMR spectroscopy. While synthetic kaolinite with a regular structure has two ^{VI}Al sites (Fenzke et al., 1984; Hayashi et al., 1992), these sites could not be distinguished in our samples due to the observed broad signals (Fig. 3). We attribute the line-shape broadening to contributions from second-order quadrupolar broadening, chemical shift anisotropy, and dipole broadening. Attempts to simulate quadrupolar coupling and the symmetry parameters were regarded as inaccurate; therefore, we limit the discussion for comparison of different chemical environments corresponding to ^{IV}Al (50–90 ppm), ^{V}Al (20–35 ppm), and ^{VI}Al (4–7 ppm) sites (Schroeder and Pruett, 1996; van Bokhoven et al., 2000; Sreeja et al., 2008; Barrow et al., 2016; Doubi et al., 2018).

The asymmetry of bands in Fig. 3 with a peak maximum at 74 ppm indicates the presence of distorted ^{IV}Al sites and/or varied chemical

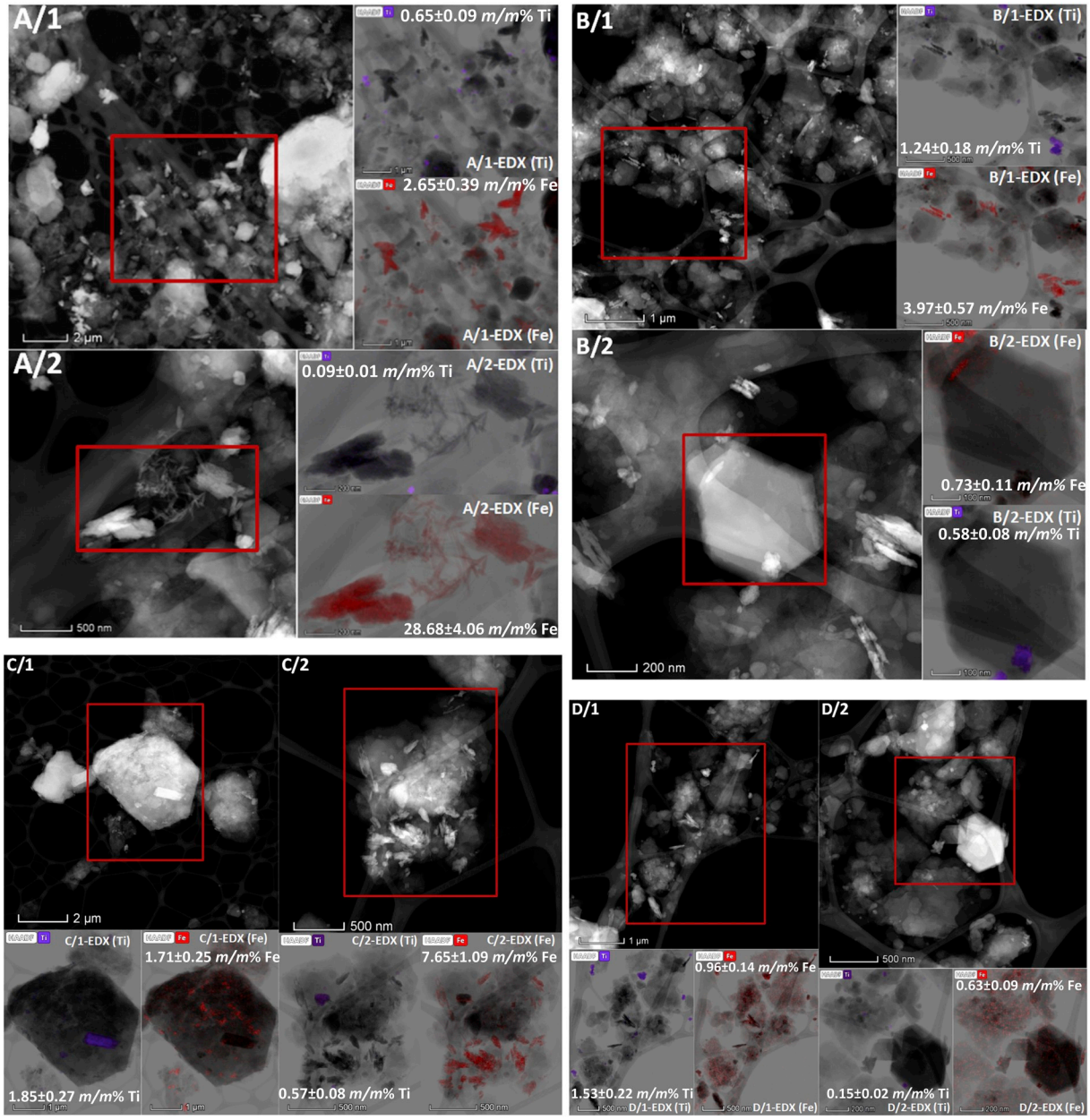

Fig. 2. Representative scanning transmission electron microscopic images of samples K (A), K-5-3 (B), K-8-3-W (C), and K-11-6 (D), along with Ti and Fe elemental distribution maps (insets below/next to in each panel, where inverse HAADF images are displayed for better visibility) from EDX measurements for the highlighted areas.

environments. Neither the increased acid concentration nor the treatment time influenced the shape and the intensity of these bands. In contrast to kaolinites with lower Fe content, the ^{IV}Al band in sample K is rather intense, as the structural iron with a greater ionic radius cause strain in the kaolinite crystal upon Al to Fe substitution at the octahedral site. However, based on the ^{27}Al CP NMR spectra, which is a surface-sensitive technique, significant differences were observed among the studied samples. The acid treatment at more accessible surfaces increased the number of ^{V}Al sites. The ^{IV}Al sites were found to be more typical for the bulk phase of the sample. Bands characteristic of ^{V}Al- and ^{IV}Al-coordination environments were also detected (Fig. 3) for Knano and Knano-5-6 samples. The effects of acid treatment were even more expressed for sample K-8-3. The band intensities of ^{IV}Al and ^{V}Al defect sites slightly increased with the increase of acid concentration and treatment time. Unexpectedly, we observed that the treatment with 11 M HCl for 9 h did not cause any change in the ^{27}Al CP spectrum. Since the surface accessible Al sites in the crystalline K sample was limited, the number of defect sites formed during acid treatment had to parallel this. Otherwise, the mullite phase would have appeared and the silicate structure would have collapsed. Based on ^{27}Al MAS NMR measurements, the acid treatment induced only slight modifications to the surface structure as shown by the loss of ^{VI}Al coordination and formation of ^{V}Al and ^{IV}Al sites. This parallels literature data (Alsawalha, 2016) as it suggests inertness of the silicate structure to acid treatment (Sreeja et al., 2008; Alsawalha, 2016).

3.4. Combined solid-state ^{1}H and ^{27}Al NMR measurements for the K-8-3-W sample

The atomic structure and composition of kaolinite dictate that the majority of the sOH-groups are connected to octahedral ^{VI}Al sites that form H-bonds of different strengths. The commonly used vibrational

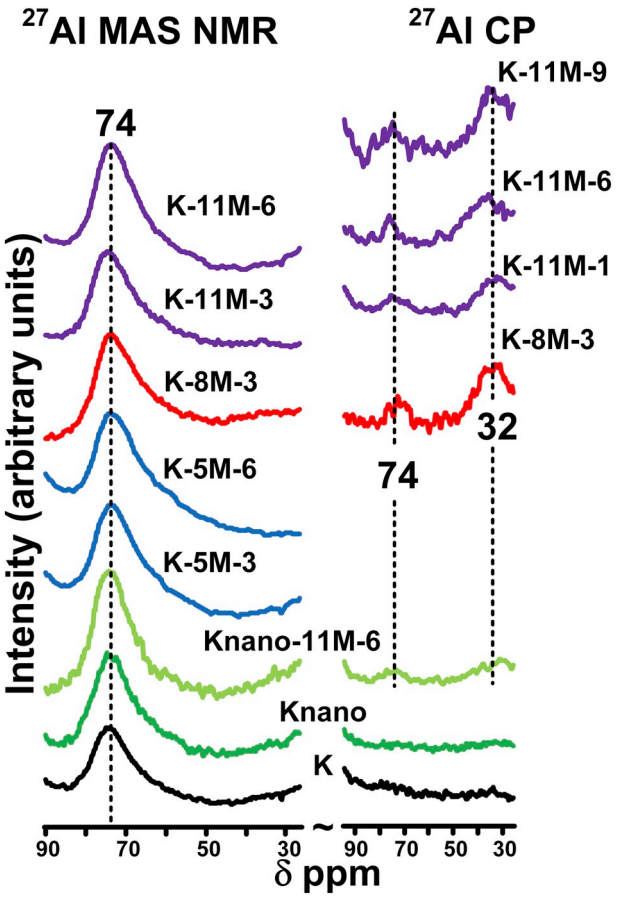

Fig. 3. The effect of acid treatment on the Al-coordination environment from ^{27}Al MAS NMR spectroscopy. The ^{27}Al CP spectra are shown as an inset on the right-hand side. Spectral ranges considered: ^{VI}Al: 4–7 ppm (not shown, ideal coordination environment); ^{V}Al defect site: 20–35 ppm; ^{IV}Al defect site: 50–80 ppm (Schroeder and Pruett, 1996; van Bokhoven et al., 2000; Sreeja et al., 2008; Barrow et al., 2016; Doubi et al., 2018).

spectroscopy of OH-groups was not feasible here due to the low surface concentration of the defect sites and the limited spectral changes due to OH-groups attached to ^{IV}Al and ^{V}Al defect sites. Therefore, the identification of OH-groups in different chemical environments was carried out by ^{1}H NMR spectroscopic technique (Knözinger and Ratnasamy, 1978; DeCanio et al., 1994; Hietala et al., 1994; Deng et al., 1997; Ertl et al., 1997; Digne et al., 2002, 2004; Chizallet et al., 2007; Wischert et al., 2011; Huittinen et al., 2011; Delgado et al., 2012; Novikova et al., 2014; Taoufik et al., 2014; Barrow et al., 2016).

The ^{1}H and ^{27}Al NMR spectra of the K-8-3-W sample after heat treatment for an additional 30 and 180 min at 400 °C are shown in Fig. 4. The ^{27}Al CP NMR spectra suggest that the heat treatment favors the formation of ^{V}Al centers at the surface (intensity increase at ~34 ppm). Our spectra show unexpectedly sharp ^{1}H peaks, which may be a result of non-restricted H^+ movement or the effective separation of H^+ environments. However, we cannot exclude the possibility if the removal of H^+ environments of the sample by the T_2 filter used for background suppression. A decrease of the relative intensity in the 4–6 ppm range of the ^{1}H spectra can also be observed in comparison to the peak of the highest intensity at 7.8 ppm. Our spectral assignments are based on the ^{1}H NMR data for γ-Al_2O_3, since to date; no assignments were made for kaolinite.

Based on the modified Knötzinger and Ratnasamy model (Knözinger and Ratnasamy, 1978; Ertl et al., 1997; Tsyganenko and Mardilovich, 1996; Novikova et al., 2014; Barrow et al., 2016), there are three types of OH-environments on the surface of γ-Al_2O_3. The terminal OH connected to the Al-center (μ^1 or OH_n) has a basic character and gives an NMR signal in the 0.2–0.5 ppm range. The bridging-OH (μ^2 or OH_{nn}) with acidic character can be detected in the 2.2–4.0 ppm range. The most acidic OH is coordinated to three Al sites (μ^3 or OH_{nnn}) in addition to being involved in H-bonding that give rise to the *ca.* 4 ppm signal. The latter can also be at as high as 14 ppm (Knözinger and Ratnasamy, 1978; DeCanio et al., 1994; Hietala et al., 1994; Deng et al., 1997; Ertl et al., 1997; Digne et al., 2002, 2004; Chizallet et al., 2007; Wischert et al., 2011; Huittinen et al., 2011; Delgado et al., 2012; Novikova et al., 2014; Taoufik et al., 2014; Barrow et al., 2016).

Our ^{1}H NMR spectrum of the K-8-3-W sample did not indicate the presence of terminal OH-groups with basic character (Table 1), but shows the μ^3-acidic and strongly acidic (δ_{OH} = 3.3–5.3 ppm) groups, in addition to the H-bonded strongly acidic (δ_{OH} 5.3–9.2 ppm) groups. Tentatively, we assigned the 9.2 ppm peak in the ^{1}H NMR spectrum to an OH-group in a structural iron-environment in the K-8-3-W sample. Detailed ^{1}H NMR study of the surface OH-groups and adjacent to ^{V}Al and ^{IV}Al centers are planned.

3.5. Porosity and temperature programmed desorption (TPD) studies

The specific surface area (SSA) and porosity data of the samples studied are summarized in Table 2. As a photocatalyst standard, the SSA and porosity data of the Degussa P25 TiO_2 sample were also determined. The main phase in K was book-type kaolinite, in addition to the presence of hematite, goethite, quartz, and illite. Knano contained hematite, goethite, book-type kaolinite phases and molecular TO-sheets (exfoliation efficiency at most 38%). Given the considerably higher efficiency of precursor formation (92–94%), first (K + EG, 92–94%), and second exchange intercalation efficiency (K + HA, 96%), the low yield of exfoliation was unexpected. We attribute this to the anomalous behavior of intercalated samples due to the presence of colloidal iron co-mineral particles on the length scale of few nanometers, which can intercalate the HA expanded kaolinite (basal distance is *ca.* 2.6 nm). A similar phenomenon (Chen et al., 2013) was taken advantage of in pillaring montmorillonite with TiO_2 particles.

The BET SSA and porosity data of the acid-treated samples showed only slight variations. An exception was the average pore diameter, which increased as the result of acid treatment leading to advantageous catalytic activity in comparison to the TiO_2 standard (Table 2). As described below, the acid treatment significantly increased the photocatalytic activity, which could not be interpreted solely based on the N_2 adsorption data. Rather, the oxalic acid decomposition efficiency was likely due to the surface concentration, distribution, and degree of crystallinity of the iron contaminants, as well as to the acid/base nature of the surface (see the photochemical data in Table 3).

The acid/base character of the kaolinite surface was studied using the TPD technique (Fig. 5). Table 3 also displays the photochemical oxalate decomposition efficiency data from permanganometric titrations. The pre-treatment temperature prior to TPD measurements was found to be important. At low pre-treatment temperature, the coordinated Zundel ($H_5O_2^+$ core)- and/or the Eigen (H_3O^+ core)-type water can be desorbed simultaneously with the test gas between 200 and 350 °C. High pre-treatment temperature can cause partial dehydroxylation that creates artefactual defect sites for acid treatment. We selected the pre-treatment temperature of 350 °C on the basis of thermogravimetric data (Vágvölgyi et al., 2020). Another caveat of the analysis was that the TPD curves of samples K and Knano could not be used as standards for the acid-treated derivatives due to their different phase compositions.

From Fig. 5, the ammonia bonding sites can be characterized by a broad desorption band and a single temperature maximum. The interpretation of CO and CO_2 desorption curves were challenging due to their ill-defined inflection points and asymmetric shapes. The amphoteric and alkaline bonding sites (as measured by CO and CO_2 adsorption, respectively) presented a similar population (below 10 μmol/g),

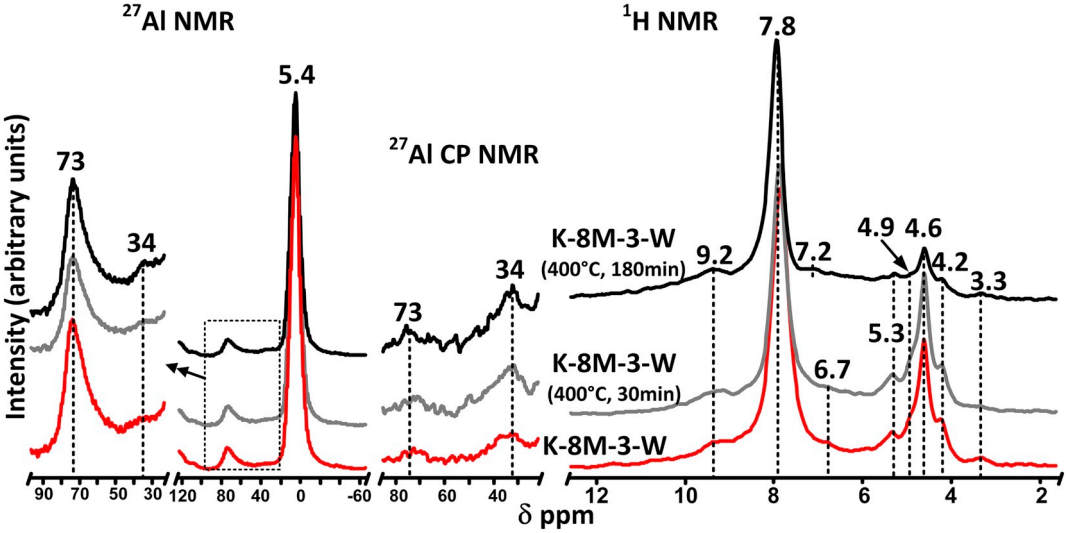

Fig. 4. Solid State ^{27}Al and ^{1}H NMR spectra of sample K-8-3-W and heat-treated derivatives. Spectral ranges considered: ^{VI}Al: 4–7 ppm; ^{V}Al defect site: 20–35 ppm; ^{IV}Al defect site: 50–80 ppm (Schroeder and Pruett, 1996; van Bokhoven et al., 2000; Sreeja et al., 2008; Barrow et al., 2016; Doubi et al., 2018).

Table 1
Summary of ^{1}H NMR spectroscopic data (ppm) based on the reference γ-Al_2O_3. assignments. ^{n}Al designates aluminum ion of ill-determined coordination environment, such as mixture of ^{IV}Al, ^{V}Al, and ^{VI}Al.

Assignment	δ_{OH} /exp. [28]	δ_{OH} /calc. [31]	δ_{OH} /exp. [37]
HO-μ^1-^{IV}Al	−0.2	0.3	−0.3; 0.5
H_2O - ^{V}Al, ^{V}Al; H-bond donor		0.5	
μ^1 - ^{IV}Al H-bond acceptor		1.9–1.3	
HO-μ^2-^{VI}Al, ^{n}Al	2.3–0.8	2.9–1.6	2.2
HO-μ^2-^{V}Al, ^{n}Al	2.2–1.5		
HO-μ^2-^{IV}Al, ^{n}Al	2.5–1.9		
HO-μ^3- (^{n}Al)$_3$	4.0–2.5		4.3
μ^3-^{IV}Al, ^{VI}Al, ^{VI}Al		4.5	
μ^1 - H_2O, ^{V}Al		4.3	
μ^1- H_2O, ^{V}Al; H-bond donor		14.2	
μ^3 - ^{IV}Al, ^{VI}Al, ^{VI}Al; H-bond donor		11.8	
μ^2 - ^{IV}Al, ^{V}Al; H-bond donor		14.9	

Table 2
The effect of acid treatment on the specific surface area (SSA) and the porosity of the samples (micro-pores less than 2 nm, meso-pores between 2 and 50 nm, and macro-pores above 50 nm) for the studied kaolin (Felsőpetény, Hungary) samples.

Designation	F_{BET} m^2/g	F_{BJH} m^2/g	F_{micro} m^2/g	V_{micro} cm^3/g	$V_{all\ pores}$ cm^3/g	$D_{average}$ nm
K	16.9	15.5	2.1	0.0009	0.0556	11.6
Knano	16.5	18.0	n.a	n.a.	0.0608	12.2
Knano-11-6	12.0	12.0	0.7	0.0002	0.0378	12.4
K-11-1	14.4	14.0	1.7	0.0007	0.0556	15.8
K-11-3	14.3	14.0	1.5	0.0006	0.0555	15.8
K-11-6	14.1	14.4	1.2	0.0004	0.0504	14.0
K-8-3-W	15.3	14.0	2.1	0.0010	0.0550	15.7
K-5-1	16.0	15.0	3.0	0.0013	0.0553	14.9
K-5-3	17.3	15.7	3.1	0.0013	0.0586	14.9
K-5-6	14.1	15.3	0.8	0.0002	0.0567	14.9
K-5-1-W	15.5	13.9	2.1	0.0009	0.0548	15.8
K-5-3-W	14.7	13.0	2.7	0.0012	0.0530	16.3
K-5-6-W	14.0	14.0	1.8	0.0007	0.0532	15.7
TiO_2	45.0	48.0	2.0	0.0005	0.1779	14.8

while the number of acidic sites (measured by NH_3 adsorption) was less than 20 μmol/g. Considering the porosity (Table 2) and TPD (Fig. 5) measurements of the acid-treated (using 5 and 11 M HCl) and washed samples, we propose that the quantity, distribution, and morphology of the iron contaminants on the surface adopt optimal values with respect to photochemical activity. Therefore, we consider sample K-8-3-W being optimal for photochemical oxalate decomposition studies. We anticipate that the employed additional wetting and drying by exposure to air favor a desirable morphology.

The CO-TPD curves for H_2-treated samples (Fig. 5D) indicated the formation of H_2 due to the presence of negative features due to the difference in heat conductivity of He and H_2 gases (0.151 and 0.181 $W{\cdot}m^{-1}{\cdot}K^{-1}$, respectively). Exceptions were the K-11 samples, where all surface-exposed Fe contents were eliminated. A similar phenomenon was already reported for modified zeolites (Lónyi et al., 2009), in which sOH-groups with strong acidity can oxidize Pt and evolve H_2 gas. Since the TCD detector is not selective to gas composition, it was not possible to determine the amount of H_2 formed from these measurements. The TPD curves of K, Knano, and K-11 samples under non-reduced conditions in Fig. 5C shows that CO desorption was a prolonged process in 100–300 °C range, thus, we anticipate simultaneous desorption of CO and H_2 gases. The presence of H_2 evolution is significant, since it indirectly confirmed that the acid-treated samples contain strong Brønsted acid sites in agreement with ^{1}H NMR measurements. Due to the strong Lewis acid character of the structural Fe, we anticipate that the strongest osOH-groups are located at the Al to Fe substitution sites.

As a demonstration of reproducibility, seven parallel K-8-3-W samples were prepared by the acid treatment of different batches of kaolin. The results of the ICP analyses and the decomposition efficiencies are summarized in Table 4. Well-reproducible decomposition efficiency of 95 ± 1% was obtained for a range of surface iron concentration of 0.9–2.2% (*m/m*) in Fe atom. A reproducible amount of dissolved Al^{3+} (0.1% (*m/m*) in Al atom) was measured due to exchange with Fe^{3+} at the TO-sheet edges (Jia et al., 2019) (see above in Section 3.1.).

Overall, the photochemically best performing K-8-3-W sample contained acidic and basic sites in equal amounts and low populations, as can be concluded from TPD data in Table 3. From the catalytic point of view, it is interesting that the peak maximum of the desorption curve was found to be significantly lower (161 *vs.* 151 °C) for K-8-3-W than for any other samples. This was an indication for the presence of a considerably lower amount of binding sites for the oxalate relative to the other acid-treated samples, which created a competition among the adsorbing molecules for the active site. We hypothesize that better adsorption may limit the desorption of the reaction products from the

Table 3
A summary of temperature programmed desorption data and photochemical decomposition efficiency of oxalic acid (η%, λ_{max} = 365 nm) using various acid treated natural kaolin samples.

	T_{max}, °C	ΣNH$_3$ mmol/g	T_{max}, °C	ΣCO mmol/g	T_{max}, °C	CO$_2$ mmol/g	ΣCO$_2$ mmol/g	η% (COOH)$_2$
K	185	0.026	159	0.026	86 & 181	0.001 & 0.009	0.010	10–25
Knano	186	0.007	158	0.012	83 & 163	0.001 & 0.011	0.012	10–20
K-11-3	180	0.011	187	0.008	87 & 180	0.001 & 0.003	0.004	29–34
K-11-6	173	0.01	185	0.005	90 & 201	< 0.00 & 0.003	0.003	30–65
K-8-3-W	161	0.006	–	–	151	0.006	0.006	94–96
K-5-3	187	0.015	191	0.009	88 & 183	0.001 & 0.009	0.010	29–42
K-5-6	184	0.016	197	0.006	87 & 200	< 0.00 & 0.006	0.006	65–92
K-5-3-W	184	0.017	167	0.008	93 & 190	< 0.00 & 0.004	0.004	25–91
K-5-6-W	181	0.014	187	0.004	88 & 172	< 0.00 & 0.006	0.006	42–88

surface. The reaction kinetics was briefly investigated as illustrated by Fig. 6.

It is practical to determine the percentage of oxalic acid decomposition by photochemical activation as a function of the BET surface area as a measure of efficiency. Fig. 6 compares the decomposition efficiency as a function of irradiation time for reference and acid-treated samples. We found that it took about 200 min for the untreated kaolinite (K) to exceed the efficiency of the TiO_2 standard. It was also evident that acid treatment enhances oxalic acid decomposition in comparison to the TiO_2 or untreated kaolinite reference sample. The above trends are remarkable given that the kaolin samples have a lower surface area (12.0–17.3 m^2/g) relative to the TiO_2 reference (45.0 m^2/g) and thus the reaction time should increase in order to decompose the same amount of oxalic acid. While the K-5-6-W sample shows a slightly better oxalate decomposition yield, we only found the acid treatment procedure and sample handling employed for the K-8-3-W sample to be reproducible.

3.6. Influence of heat treatments on photochemical activity of K-8-3-W

The increase of the photochemical activity of the acid-treated samples can be correlated with the presence of defect sites with lowered Al coordination numbers, or the co-minerals (goethite and anatase). An unknown here is the differences in morphology and structural defects attributed to the broken bonds involving bridging oxide groups and the Al substitution for Si in tetrahedral sheets (Zhang et al., 2014). However, additional defect sites can be produced by thermal treatment of the best performing K-8-3-W sample by heating kaolinite samples and achieving complete dehydration and partial dehydroxylation (up to 5% at 400 °C) (Zsirka et al., 2017b).

Table 4
Summary of dissolved and surface Fe ions, dissolved Al ion concentration from ICP measurements, and the photochemical degradation efficiency (η%, λ_{max} = 365 nm) of oxalic acid of seven parallel K-8-3-W samples.

Runs	Dissolved Fe % (*m*/*m*)	Surface Fe%, (*m*/*m*)		Dissolved Al, % (*m*/*m*)	η% (COOH)$_2$
		in Fe	in Fe_2O_3		
1	3.49	0.97	4.99	0.105	93
2	2.80	1.66	4.00	0.103	93
3	2.29	2.17	3.28	0.108	95
4	2.68	1.78	3.83	0.099	96
5	2.97	1.50	4.24	0.103	94
6	2.50	1.96	3.57	0.100	96
7	2.90	1.56	4.14	0.101	96
Avg.	2.80	1.66	4.01	0.103	95
σ	0.38	0.38	0.55	0.003	1

Fig. 7 shows the decomposition efficiencies for K-8-3-W and its heat-treated derivatives using oxalic acid as an electron acceptor. A second-order polynomial trend ($\eta\% = 0.0013\,min^{-2}t^2 + 0.058\,min^{-1}t + 4.8\%$, R^2 = 99.8%, where *t* represents irradiation time) was established for the reference, non-heat treated K-8-3-W sample with low SSA values and/or controlled diffusion of oxalate to the photocatalytically active centers. Moreover, the decomposition profile of a sample treated at 400 °C for 30 min showed similarity to the reference sample. We

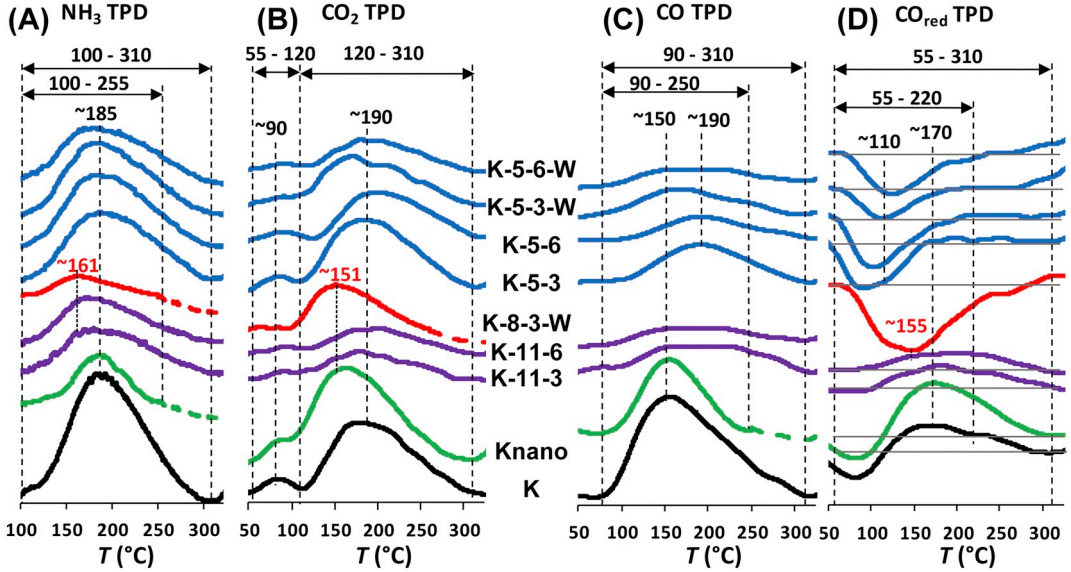

Fig. 5. Temperature programmed desorption (TPD) curves recorded for investigating the acid/base properties of treated samples using NH_3, CO_2, CO; and H_2 reducing gas followed by CO probe gases. Dashed lines indicate correction due to the evolution of Zundel- and Eigen-type waters.

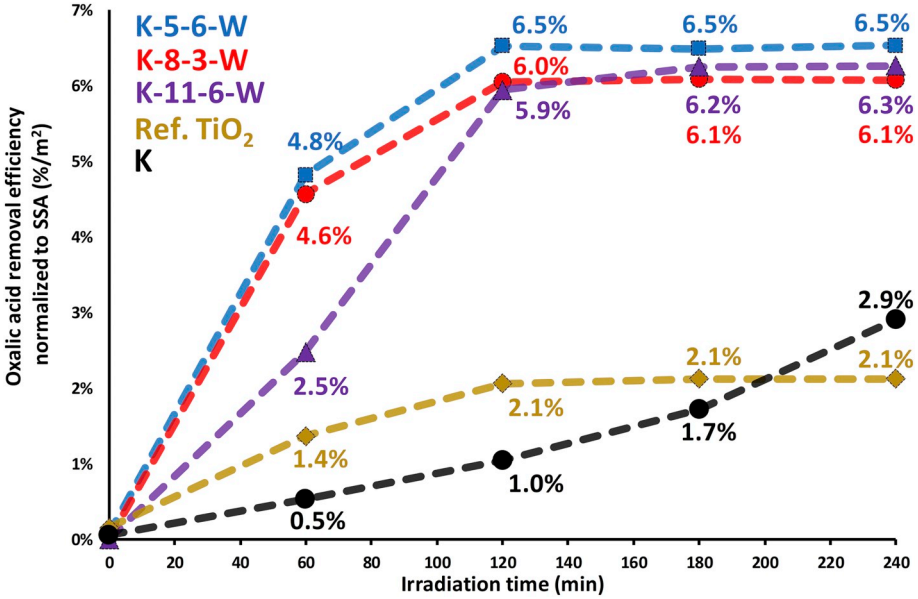

Fig. 6. Photochemical decomposition efficiencies of oxalic acid normalized to SSA values of selected acid-treated kaolin samples, untreated kaolin, and reference Degussa P25 TiO_2 standard. Error bars of measurement are ± 0.2%.

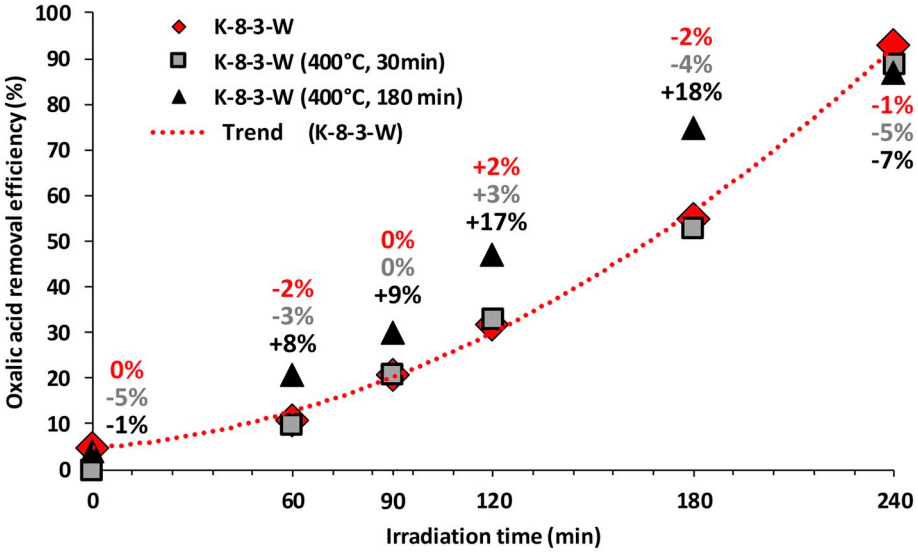

Fig. 7. Photochemical decomposition efficiency of sample K-8-3-W and its heat-treated derivatives as a function of the irradiation time using $(COOH)_2$ as electron acceptor. The efficiency values shown adjacent to the data points are deviations from the trendline fitted for K-8-3-W. Error bars of measurement are ± 2%.

rationalize the increased decomposition efficiency observed for the K-8-3-W (400 °C, 180 min) heat-treated sample by the increase of the population of photochemically active centers. We propose that the presence of ^{IV}Al and ^{V}Al defect sites at the kaolinite surface have a significant influence on photochemical decomposition efficiency in addition to the presence of Fe/Ti-containing co-minerals. The quantity of the defect sites can be tuned with a cautious selection of the temperature and the duration of heat treatment.

4. Conclusion

In order to advance the kaolin's potential as a photocatalyst, correlations between the surface properties and the photochemical activity were established. Surface modification of natural kaolins containing goethite, hematite, and anatase co-minerals can be achieved using aqueous HCl solutions of varying concentrations and treatment periods. We established that the acid treatment does not deteriorate the aluminosilicate matrix; however, it generates low coordinate Al sites. By varying the acid concentration and the duration of the treatment, the surface concentration and morphology of the iron co-minerals can be tuned, leading 95% oxalic acid decomposition, importantly, in a reproducible manner. The photochemical activity of natural kaolins is generally not well reproducible, but washing and drying in addition to the acid or heat treatment can enhance the reproducibility of photochemical activity.

Our best performing kaolin sample (K-8-3-W) from the natural red kaolin of Felsőpetény, Hungary, was prepared by 3 h exposure to 8 M $HCl_{(aq)}$ solution followed by washing, drying for 24 h, and grinding. TEM images showed that the acid treatment influences the surface concentration (1.7 ± 0.4%, weight of Fe atom/weight of K-8-3-W sample) and distribution of the iron-containing co-minerals in kaolin. The co-minerals formed *ca.* ~500 nm loosely associated clusters of particles. Minor differences in the SSA and porosity data of the acid-treated samples were documented, while slight increases were detected

in the pore diameter. We wish to point out that the acid/base character of the surface from temperature-programmed desorption studies did not correlate with the acidification process, ^{1}H NMR results, or the observed photochemical activity. Furthermore, vibrational spectroscopic techniques commonly used for the characterization of oxide-type catalysts are of limited use due to high surface OH-group concentration, and the simultaneous presence of contaminants with H-donor/acceptor interactions. Despite these challenges, we conclude that the presence of ^{IV}Al and ^{V}Al defect sites in addition to the presence of Fe/Ti-containing co-minerals are of mechanistic importance for photochemical activity.

Declaration of Competing Interest

The authors declare that they have no known competing financial interests or personal relationships that could have appeared to influence the work reported in this paper.

Acknowledgement

Access to powder X-ray diffraction, NMR spectroscopic and TEM (Nanolab) microscopic instrumentation at the University of Pannonia is acknowledged. The authors thank Lighttech GmbH (Dunakeszi, Hungary) for the UV lamps and the Agyag-Ásvány GmbH (Felsőpetény, Hungary) for the kaolin samples. Financial supports from the GINOP-2.3.2-15-2016-00016 and GINOP-2.3.2-15-2016-00053 projects (co-financed by the Széchenyi 2020 program) are also acknowledged.

References

Ajemba, R.O., Ugonabo, V.I., Igbokwe, P.K., Onukwuli, O.D., 2013. Analysis of Nitric Acid Activated Ukpor Kaolin : Structural Transformations and Adsorptive Properties. 7. pp. 2241–2250.

Alsawalha, M., 2016. Properties and characterizations of different natural jordanian materials. Am. J. Mater. Sci. 6, 87–90. https://doi.org/10.5923/j.materials.20160604.01.

Barrow, N.S., Scullard, A., Collis, N., 2016. Surface selective ^{1}H and ^{27}Al MAS NMR observations of strontium oxide doped γ-alumina surface binding sites of strontium oxide on γ-alumina identified for the first time. Johnson Matthey Technol. Rev. 60, 90–97. https://doi.org/10.1595/205651316X690943.

Bergaya, F., Theng, B.K.G., Lagaly, G., 2006. Handbook of clay Science. 1248. Elsevier Ltd., pp. 1–1248. https://doi.org/10.1017/CBO9781107415324.004.

Bryant, S.L., Buller, D.C., 1990. Formation damage from acid treatments. SPE Prod. Eng. 5, 455–460. https://doi.org/10.2118/17597-PA.

Chen, D., Du, G., Zhu, Q., Zhou, F., 2013. Synthesis and characterization of TiO_2 pillared montmorillonites: Application for methylene blue degradation. J. Colloid Interface Sci. 409, 151–157. https://doi.org/10.1016/j.jcis.2013.07.049.

Chizallet, C., Costentin, G., Lauron-Pernot, H., Che, M., Bonhomme, C., Maquet, J., 2007. Study of the structure of OH groups on MgO by 1D and 2D ^{1}H MAS NMR combined with DFT cluster calculations. J. Phys. Chem. C 111, 18279–18287. https://doi.org/10.1021/jp077089g.

Conley, R.F., Althoff, A.C., 1971. Surface acidity in kaolinites. J. Colloid Interface Sci. 37, 186–195. https://doi.org/10.1016/0021-9797(71)90279-7.

DeCanio, E.C., Edwards, J.C., Bruno, J.W., 1994. Solid-State ^{1}H MAS NMR characterization of γ -alumina and modified γ -aluminas. J. Catal. 148, 76–83.

Delgado, M., Delbecq, F., Santini, C.C., Lefebvre, F., Norsic, S., Putaj, P., 2012. Evolution of structure and of grafting properties of γ -alumina with pretreatment temperature. J. Phys. Chem. C 834–843. https://doi.org/10.1021/jp208709x.

Deng, F., Wang, G., Du, Y., Ye, C., Kong, Y., Li, X., 1997. ^{1}H MAS and ^{1}H {^{23}Na} double resonance NMR studies on the modification of surface hydroxyl groups of γ-alumina by sodium. Solid State Nucl. Magn. Reson. 2040, 281–290.

Digne, M., Sautet, P., Raybaud, P., Euzen, P., Toulhoat, H., 2002. Hydroxyl groups on γ -alumina surfaces : a DFT study. J. Catal. 5, 1–5. https://doi.org/10.1006/jcat.2002.3741.

Digne, M., Sautet, P., Raybaud, P., Euzen, P., Toulhoat, H., 2004. Use of DFT to achieve a rational understanding of acid – basic properties of γ -alumina surfaces. J. Catal. 226, 54–68. https://doi.org/10.1016/j.jcat.2004.04.020.

Ding, Z., Zhu, H.Y., Lu, G.Q., Greenfield, P.F., 1999. Photocatalytic properties of titania pillared clays by different drying methods. J. Colloid Interface Sci. 209, 193–199. https://doi.org/10.1006/jcis.1998.5857.

dos Santos, L.R., Mascarenhas, A.J.S., Silva, L.A., 2017. Preparation and evaluation of composite with a natural red clay and TiO_2 for dye discoloration assisted by visible light. Appl. Clay Sci. 135, 603–610. https://doi.org/10.1016/j.clay.2016.11.002.

Doubi, H.G., Montouillout, V., Lecomte Nana, G.L., Nait Ali, B., Konan, L.K., Smith, A., 2018. ^{29}Si and ^{27}Al MAS NMR characterization of the structural evolution of a lateritic clay under acidic and alkaline treatments. J. Mater. Sci. Eng. 07, 1–7. https://doi.org/10.4172/2169-0022.1000409.

Ertl, G., Knözinger, H., Weitkamp, J., 1997. The Handbook of Heterogeneous Catalysis.

Fenzke, D., Freude, D., Fröhlich, T., Haase, J., 1984. NMR intensity measurements of half-integer quadrupole nuclei. Chem. Phys. Lett. 111, 171–175. https://doi.org/10.1016/0009-2614(84)80458-3.

Fida, H., Guo, S., Zhang, G., 2015. Preparation and characterization of bifunctional Ti–Fe kaolinite composite for Cr (VI) removal. J. Colloid Interface Sci. 442, 30–38. https://doi.org/10.1016/j.jcis.2014.11.023.

Gleizes, A.N., Samélor, D., Vahlas, C., Sarou-Kanian, V., Florian, P., Massiot, D., 2014. Temperature dependent 4-, 5- and 6-fold coordination of aluminum in MOCVD-grown amorphous alumina films: from local coordination to material properties. Adv. Sci. Technol. 91, 123–133. https://doi.org/10.4028/www.scientific.net/ast.91.123.

Gupta, V.K., Jain, R., Mittal, A., Mathur, M., Sikarwar, S., 2007. Photochemical degradation of the hazardous dye Safranin-T using TiO_2 catalyst. J. Colloid Interface Sci. 309, 464–469. https://doi.org/10.1016/j.jcis.2006.12.010.

Hayashi, S., Ueda, T., Hayamizu, K., Akiba, E., 1992. NMR study of kaolinite. 1. ^{29}Si, ^{27}Al, and ^{1}H spectra. J. Phys. Chem. 96, 10922–10928.

Hietala, J., Root, A., Knuuttila, P., 1994. The Surface acidity of pure and modified aluminas in Re/Al_2O_3 metathesis catalysts as studied by 1H MAS NMR spectroscopy and its importnace in the ethenolysis of 1,5-cyclooctadiene. J. Catal. 46–55.

Hou, S.S., Beyer, F.L., Schmidt-Rohr, K., 2002. High-sensitivity multinuclear NMR spectroscopy of a smectite clay and of clay-intercalated polymer. Solid State Nucl. Magn. Reson. 22, 110–127. https://doi.org/10.1006/snmr.2002.0075.

Huittinen, N., Sarv, P., Lehto, J., 2011. A proton NMR study on the specific sorption of yttrium(III) and europium(III) on gamma-alumina [γ-Al_2O_3]. J. Colloid Interface Sci. 361, 252–258. https://doi.org/10.1016/j.jcis.2011.05.055.

Jepson, W.B., Rowse, J.B., 1975. The composition of kaolinite: an electron microscope microprobe study. Clay Clay Miner. 23, 310–317.

Jia, X., Cheng, H., Zhou, Y., Zhang, S., Liu, Q., 2019. Time-efficient preparation and mechanism of methoxy-grafted kaolinite via acid treatment and heating. Appl. Clay Sci. 174, 170–177. https://doi.org/10.1016/j.clay.2019.04.001.

Kibanova, D., Trejo, M., Destaillats, H., Cervini-Silva, J., 2011. Photocatalytic activity of kaolinite. Catal. Commun. 12, 698–702. https://doi.org/10.1016/j.catcom.2010.10.029.

Knözinger, H., Ratnasamy, P., 1978. Catalytic aluminas: surface models and characterization of surface sites. Catal. Rev. 17, 31–70. https://doi.org/10.1080/03602457808080878.

Kumar, S., Panda, A.K., Singh, R.K., 2013. Preparation and characterization of acid and alkaline treated kaolin clay. Bull. Chem. React. Eng. Catal. 8, 61–69. https://doi.org/10.9767/bcrec.8.1.4530.61-69.

Liu, Z., Wang, J., Ma, H., Cheng, L., Ar, S., Yang, J., 2018. A new natural layered clay mineral applicable to photocatalytic hydrogen production and/or degradation of dye pollutant. Environ. Prog. Sustain. Energy 37, 1003–1010. https://doi.org/10.1002/ep.12775.

Lónyi, F., Kovács, A., Szegedi, A., Valyon, J., 2009. Activation of hydrogen and hexane over pt,h-mordenite hydroisomerization catalysts. J. Phys. Chem. C 113, 10527–10540. https://doi.org/10.1021/jp810716f.

da Lopes, J.S., Rodrigues, W.V., Oliveira, V.V., do Braga, A.N.S., da Silva, R.T., França, A.A.C., da Paz, E.C., Osajima, J.A., da Silva Filho, E.C., 2019. Modification of kaolinite from Pará/Brazil region applied in the anionic dye photocatalytic discoloration. Appl. Clay Sci. 168, 295–303. https://doi.org/10.1016/j.clay.2018.11.028.

Menager, M., Sarakha, M., 2012. Simulated solar light phototransformation of organophosphorus azinphos methyl at the surface of clays and goethite. Environ. Sci. Technol. 47, 765–772. https://doi.org/10.1021/es301866f.

Novikova, L., Roessner, F., Belchinskaya, L., Alsawalha, M., Krupskaya, V., 2014. Study of surface acid–base properties of natural clays and zeolites by the conversion of 2-methylbut-3-yn-2-ol. Appl. Clay Sci. 101, 229–236. https://doi.org/10.1016/j.clay.2014.08.005.

Panda, A.K., Mishra, B.G., Mishra, D.K., Singh, R.K., 2010. Effect of sulphuric acid treatment on the physico-chemical characteristics of kaolin clay. Colloids Surf. A Physicochem. Eng. Asp. 363, 98–104. https://doi.org/10.1016/j.colsurfa.2010.04.022.

Schroeder, P.A., Pruett, R.J., 1996. Fe ordering in kaolinite; insights from ^{29}Si and ^{27}Al MAS NMR spectroscopy. Am. Mineral. 81, 26–38. https://doi.org/10.2138/am-1996-1-204.

Solyman, S.M., Betiha, M.A., 2014. The performance of chemically and physically modified local kaolinite in methanol dehydration to dimethyl ether. Egypt. J. Pet. 23, 247–254. https://doi.org/10.1016/j.ejpe.2014.08.001.

Sreeja, V., Smitha, T.S., Nand, D., Ajithkumar, T.G., Joy, P.A., 2008. Size dependent coordination behavior and cation distribution in $MgAl_2O_4$ nanoparticles from ^{27}Al Solid State NMR studies. J. Phys. Chem. C 112, 14737–14744. https://doi.org/10.1021/jp800412k.

Stebbins, J.F., Kroeker, S., Keun Lee, S., Kiczenski, T., 2000. Quantification of five- and six-coordinated aluminum ions in aluminosilicate and fluoride-containing glasses by high-field, high-resolution ^{27}Al NMR. J. Non-Cryst. Solids 275, 1–6. https://doi.org/10.1016/S0022-3093(00)00270-2.

Szabó, P., Zsirka, B., Fertig, D., Horváth, E., Csizmadia, T., Kristóf, J., 2017. Delaminated kaolinites as potential photocatalysts: Tracking degradation of Na-benzenesulfonate test compound adsorbed on the dry surface of kaolinite nanostructures. Catal. Today 287, 37–44. https://doi.org/10.1016/j.cattod.2017.01.051.

Szczepanik, B., Rogala, P., Słomkiewicz, P.M., Banaś, D., Kubala-Kukuś, A., Stabrawa, I., 2017. Synthesis, characterization and photocatalytic activity of TiO_2-halloysite and Fe_2O_3-halloysite nanocomposites for photodegradation of chloroanilines in water. Appl. Clay Sci. 149, 118–126. https://doi.org/10.1016/j.clay.2017.08.016.

Taoufik, M., Szeto, K.C., Merle, N., Rosal, D., Maron, L., Trøbosc, J., Tricot, G., Gauvin, R.M., Delevoye, L., 2014. Heteronuclear NMR spectroscopy as surface-selective technique : a unique look at the hydroxyl groups of γ-Alumina. Chem. Eur. J. 1–10.

https://doi.org/10.1002/chem.201304883.
Tsyganenko, A.A., Mardilovich, P.P., 1996. Structure of alumina surfaces. J. Chem. Soc. Faraday Trans. 92, 4843–4852. https://doi.org/10.1039/ft9969204843.
Ulicna, K., Stepánkova, H., Rimal, V., 2013. NMR study of aluminium coordination in clays. WDS'13 proceeding contrib. Pap 6, 104–109.
Üzüm, Ç., Shahwan, T., Eroğlu, A.E., Hallam, K.R., Scott, T.B., Lieberwirth, I., 2009. Synthesis and characterization of kaolinite-supported zero-valent iron nanoparticles and their application for the removal of aqueous Cu^{2+} and Co^{2+} ions. Appl. Clay Sci. 43, 172–181. https://doi.org/10.1016/j.clay.2008.07.030.
Vágvölgyi, V., Győrfi, K., Zsirka, B., Horváth, E., Kristóf, J., 2020. The role of thermal analysis in the development of high-iron-content kaolinite-based photocatalysts. J. Therm. Anal. Calorim. 11. https://doi.org/10.1007/s10973-020-09350-2.
van Bokhoven, J.A., Koningsberger, D.C., Kunkeler, P., van Bekkum, H., Kentgens, A.P.M., 2000. Stepwise dealumination of zeolite beta at specific T-sites observed with ^{27}Al MAS and ^{27}Al MQ MAS NMR. J. Am. Chem. Soc. 122, 12842–12847. https://doi.org/10.1021/ja002689d.
Wischert, R., Copéret, C., Delbecq, F., Sautet, P., 2011. Optimal water coverage on alumina : a key to generate Lewis acid – base pairs that are reactive towards the C - H bond activation of methane. Angew. Chen. Int. Ed. 3202–3205. https://doi.org/10.1002/anie.201006794.
Zhang, Y., Liu, Q., Xiang, J., Zhang, S., Frost, R.L., 2014. Insight into morphology and structure of different particle sized kaolinites with same origin. J. Colloid Interface Sci. 426, 99–106. https://doi.org/10.1016/j.jcis.2014.03.057.
Zhu, B.-L., Qi, C.-L., Zhang, Y.-H., Bisson, T., Xu, Z., Fan, Y.-J., Sun, Z.-X., 2019. Synthesis, characterization and acid-base properties of kaolinite and metal (Fe, Mn, Co) doped kaolinite. Appl. Clay Sci. 179, 105138. https://doi.org/10.1016/j.clay.2019.105138.
Zsirka, B., Horváth, E., Makó, E., Kurdi, R., Kristóf, J., 2015. Preparation and characterization of kaolinite nanostructures: Reaction pathways, morphology and structural order. Clay Miner. 50, 329–340. https://doi.org/10.1180/claymin.2015.050.3.06.
Zsirka, B., Horváth, E., Szabó, P., Juzsakova, T., Szilágyi, R.K., Fertig, D., Makó, É., Varga, T., Kónya, Z., Kukovecz, Á., Kristóf, J., 2017a. Thin-walled nanoscrolls by multi-step intercalation from tubular halloysite-10 Å and its rearrangement upon peroxide treatment. Appl. Surf. Sci. 399, 245–254. https://doi.org/10.1016/j.apsusc.2016.12.053.
Zsirka, B., Táborosi, A., Szabó, P., Szilágyi, D., Horváth, E., Juzsakova, T., Fertig, É., Kristóf, J., 2017b. Surface characterization of mechanochemically modified exfoliated halloysite nanoscrolls. Langmuir. 33, 3534–3547. https://doi.org/10.1021/acs.langmuir.6b04606.